Sensitivity of neutron observables to the model input in simulations of ^{252}Cf(sf)

J. Randrup,[1,2] P. Talou,[3] and R. Vogt[4,5]

[1]*Nuclear Science Division, Lawrence Berkeley National Laboratory, Berkeley, California 94720, USA*
[2]*Nuclear Engineering Department, University of California, Berkeley, California 94720, USA*
[3]*Nuclear Theory Group and X-Computational Physics Division, Los Alamos National Laboratory, Los Alamos, New Mexico 87545, USA*
[4]*Physics Division, Lawrence Livermore National Laboratory, Livermore, California 94551, USA*
[5]*Physics Department, University of California, Davis, California 95616, USA*

Within the framework of FREYA event-by-event fission simulations, we study the sensitivity of various neutron observables to the input yield function $Y(A, Z, \mathrm{TKE})$ on which the fission event sampling is based. We first perform a statistical analysis of the available fission data in order to determine the distribution of possible yield functions $Y(A, Z, \mathrm{TKE})$ and we then construct a sample of 15 000 such yield functions. For each of these, FREYA is used to generate one million fission events, leading to a corresponding ensemble of fission observables, including the neutron multiplicity distribution and its factorial moments, the neutron energy spectrum, and the neutron-neutron angular correlation. This procedure allows us to study the sensitivity of those neutron observables to the uncertainty in the experimental data. Particular attention is given to the pronounced anticorrelation between the mean neutron multiplicity $\bar{\nu}$ and the mean total fragment kinetic energy $\overline{\mathrm{TKE}}$. Because the former observable is very well determined experimentally, it is possible to exploit that inherent anticorrelation to derive a significantly stricter tolerance on $\overline{\mathrm{TKE}}$. In addition, we study the sensitivity to the various FREYA parameters and we introduce a method for determining a A-dependent x parameter, $x(A)$, based on the measured A-dependent neutron multiplicity, $\bar{\nu}(A)$.

I. INTRODUCTION

Nuclear fission is a rich field of physics. A typical binary fission event produces two excited fragment nuclei that promptly deexcite by the emission of neutrons and photons. The resulting product nuclei and the neutron and photon ejectiles may be detected individually or in coincidence, thus presenting a wide range of possible fission observables.

The ensuing need for addressing arbitrary types of correlated fission data has led to the development of Monte Carlo simulation models that generate complete fission events [1–7]. These models typically require as input the primary fission fragment yields as a function of their mass and charge numbers as well as their total kinetic energy, denoted as $Y(A, Z, \mathrm{TKE})$. The specification of the yield function enables the code to select, event by event, the identity of the two primary fragments, their linear and angular momenta, and their excitation energies; the subsequent deexcitation processes can then be simulated. The resulting prompt neutron and photon observables are thus sensitive to the specific yield function employed.

A number of fission applications, from energy production to nonproliferation, depend strongly on the average neutron multiplicity, $\bar{\nu}$, as well as on the associated energy spectrum. For the cases most important to those applications, the value of $\bar{\nu}$ is tightly constrained; in fact, more so than any other fission-related observable. Indeed, although the corresponding fission fragment yields have been measured by many groups and are in relatively good mutual agreement for ^{252}Cf(sf),

their differences are significant enough to render them less tightly constrained than $\bar{\nu}$.

We investigate here the sensitivity of $\bar{\nu}$ and other neutron observables to the input yield function, focusing on ^{252}Cf(sf), one of the best-measured fission cases. By use of a generalized least-squares fit to the available fission yield data, we construct a distribution of yield functions consistent with the reported experimental uncertainties and we then study how the neutron observables are affected by the use of a variery of yield functions sampled from that distribution.

We particularly seek to quantify the degree to which the measured yields can constrain $\bar{\nu}$. This is an especially interesting time to undertake such an investigation because the nuclear fission community is in the process of making a new assessment of the fission fragment yields, making use of a very similar model to calculate the deexcitation of the fission fragments [8] and avoid inconsistencies in evaluated nuclear data libraries [9]. It is important to understand whether the resulting consensus will be of high-enough fidelity to provide bounds on $\bar{\nu}$ that meet the required accuracy. However, while the primary focus is thus on the constraints on $\bar{\nu}$ placed by the measured fission fragment yields, we will also study how the uncertainty in the input yield function affects other neutron observables of interest.

It should be noted that because we consider spontaneous fission, there will be neither pre-equilibrium neutron emission nor any other emission prior to scission. Furthermore, at this

point, FREYA does not consider the possibility of scission neutrons, so that all neutrons in an event have been evaporated from the fully accelerated fragments.

While we employ one particular model in our investigation, namely FREYA [2], we expect our conclusions to have general validity as to whether experimentally determined yields can place sufficiently strong constraints on $\bar{\nu}$. Because the fission model depends on certain adjustable input parameters, we will also discuss the sensitivity of our results to those parameters.

We first, in Sec. II, discuss how a χ^2 analysis of the combined experimental data on fragment mass, charge, and kinetic energy, including the associated reported uncertainties, can provide a probability distribution of possible yield functions, $\mathcal{P}[Y(A, Z, \text{TKE})]$.

In Sec. III we describe how the standard FREYA code has been modified so it can accept an ensemble of sampled yield functions as input. In Sec. IV we then study how sensitive the calculated neutron observables are to the uncertainty in the input information reflected in the ensemble of yield functions. We particularly consider the neutron multiplicity distribution $P_n(\nu)$, the energy spectrum $\chi_n(E)$ of the evaporated neutrons, and the neutron-neutron angular correlation $C_{nn}(\theta_{12})$. A preliminary account of this study was reported previously [10].

Section V focuses on the strong correlation between the mean neutron multiplicity $\bar{\nu}$ and the mean total fragment kinetic energy $\overline{\text{TKE}}$ [10,11]. Because $\bar{\nu}$ is so well determined experimentally, this inherent correlation can be exploited to reduce the uncertainty in $\overline{\text{TKE}}$. (We obtain a reduction by nearly a factor of six.) We also discuss the sensitivity of the calculated neutron observables to the FREYA model parameters (Sec. VI). Particular attention is given to the parameter x governing the division of the available excitation energy between the two fragments and we introduce a method for determining a mass-dependent x parameter, $x(A)$, based on the measured mass-dependent mean neutron multiplicity, $\bar{\nu}(A)$.

The study is then summarized and concluded (Sec. VII). Several technical derivations are relegated to the appendices to facilitate the flow of the main presentation.

II. THE ENSEMBLE OF YIELD FUNCTIONS

We have performed a least-squares statistical analysis of available experimental data on $\overline{\text{TKE}}(A)$ and $Y(A)$ for primary fission fragments. The data sets considered are listed in Table I. Unfortunately, most experimental data sets were reported with only very limited information on the associated uncertainties. Furthermore, no covariance information was ever provided. The present work is focused on the influence of the uncertainties of the input yields on the results of event-by-event simulations. For this limited purpose, we may make somewhat simplified assumptions regarding the correlations and the uncertainties. A true evaluation would require a more thorough analysis, but the main conclusions of this study are unlikely to change with a more careful experimental data analysis.

The simulation of the deexcitation of the fission fragments by sequential emission of neutrons and photons requires the knowledge of the primary fission-fragment yields with respect to mass, charge, and total kinetic energy, $Y(A, Z, \text{TKE})$.

TABLE I. The various experimental data used in this work, ordered by the publication year for each of the three data types: $Y(A)$, $\overline{\text{TKE}}(A)$, and $\sigma_{\text{TKE}}(A)$. The EXFOR entry can be used to directly access the numerical data kept at the National Nuclear Data Center [21].

First author	Year	EXFOR #	Ref.
	$Y(A)$		
Budtz-Jørgensen	1988	23175-002	[13]
Hambsch	1997	22780-002	[14]
Kozulin	2008	41581-003	[15]
Romano	2010	14259-008	[16]
Zeynalov	2011	23118-002	[17]
Göök	2014	–	[18]
	$\overline{\text{TKE}}(A_H)$		
Whetstone	1963	14101-003	[19]
Mehta	1973	23213-008	[20]
Budtz-Jørgensen	1988	23175-003	[13]
Hambsch	1997	22780-003	[14]
Kozulin	2008	41581-004	[15]
Göök	2014	–	[18]
	$\sigma_{\text{TKE}}(A_H)$		
Budtz-Jørgensen	1988	23175-003	[13]
Hambsch	1997	22780-003	[14]
Göök	2014	–	[18]

No experimental data set provides such a complete three-dimensional yield function. Therefore, we must rely on partial information to construct the full yield function. In the present case, we first construct the two-dimensional distribution $Y(A, \text{TKE})$ assuming that TKE has a Gaussian distribution for each A value,

$$Y(\text{TKE}|A) \propto \exp\left[-\frac{\text{TKE} - \overline{\text{TKE}}(A)}{2\sigma_{\text{TKE}}^2(A)}\right], \quad (1)$$

where TKE ranges from zero up the maximum Q value for the specified mass division; the normalization is $\int Y(\text{TKE}|A)\,d\text{TKE} = Y(A)$. The functions $Y(A)$, $\overline{\text{TKE}}(A_H)$, and $\sigma_{\text{TKE}}(A_H)$ are obtained from a least-squares fit to experimental data, as explained below. The charge distribution for a given fragment mass number, $Y(Z|A)$ [with $\int Y(Z|A)\,dZ = 1$], is taken from Wahl's systematics [12], which includes odd-even factors. The full yield function is then given by

$$Y(A, Z, \text{TKE}) = Y(\text{TKE}|A)\,Y(Z|A). \quad (2)$$

A. Fission fragment mass yields

The experimental data on fission fragment mass yields used in this work are listed in Table I. The documentation available on those experimental data sets is rather poor, and crude estimates and corrections were made. As shown in Fig. 1, the experimental data are relatively consistent, although the reported experimental uncertainties had to be scaled up somewhat arbitrarily.

The Göök data [18] are the most recent measurement and possibly the most accurate. We have added a 0.5% uncorrelated uncertainty for each data point, as well as a
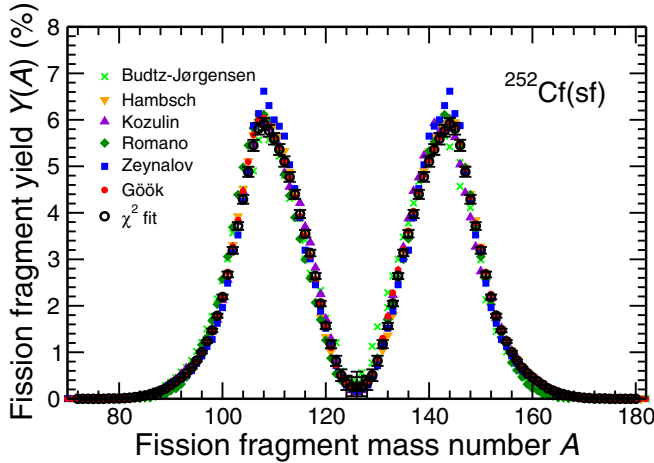
FIG. 1. Our least-squares fit (open circles with error bars) to the measured mass distribution of the primary fission fragments, $Y(A)$. The experimental data shown are from Budtz-Jørgensen et al. [13], Hambsch et al. [14], Kozulin et al. [15], Romano et al. [16], Zeynalov et al. [17], and Göök et al. [18].

5% fully correlated uncertainty on the overall normalization. Because most measurements cover a similar range of fragment masses, this normalization uncertainty vanishes during the least-squares fit procedure. The Zeynalov data [17] were reported in the ND2010 conference proceedings and only statistical uncertainties of about 1% were discussed. We have added a 5% uncertainty at each energy point. The reported uncertainties on the Romano data [16] are only statistical, we added a 2% uncorrelated uncertainty. Similarly, we added a 3% uncorrelated uncertainty to the Kozulin data [15], the Hambsch data [14], and the Budtz-Jørgensen data [13]. While all of those numbers are somewhat artificial, they are likely
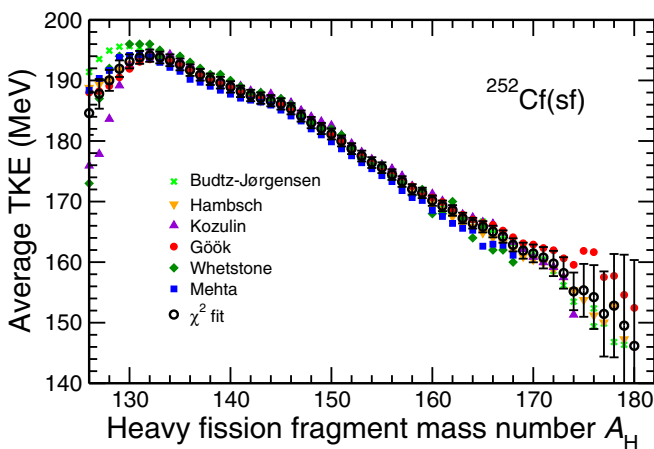
FIG. 2. Our least-squares fit (open circles with error bars) to the measured average total fragment kinetic energy as a function of the mass number of the heavy fragment, $\overline{\mathrm{TKE}}(A_H)$. The experimental data shown are from Budtz-Jørgensen et al. [13], Hambsch et al. [14], Kozulin et al. [15], Göök et al. [18], Whetstone et al. [19], and Mehta et al. [20].
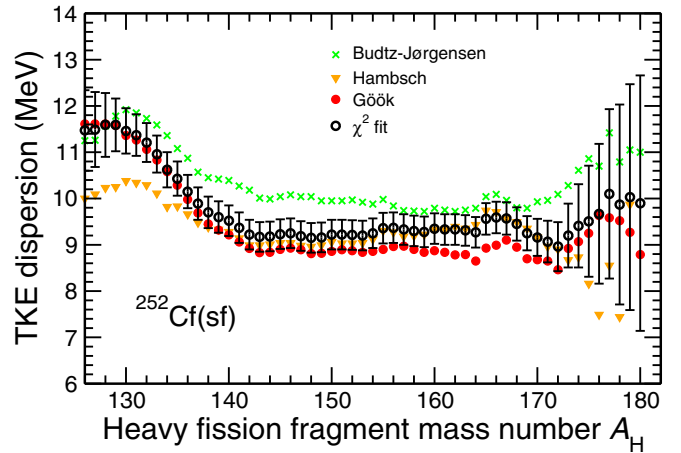
FIG. 3. Our least-squares fit (open circles with error bars) to the measured width of the TKE distribution as a function of the mass number of the heavy fragment, $\sigma_{\mathrm{TKE}}(A_H)$ [13,14,18].

on the conservative side and are not expected to influence the main conclusion of this work.

B. Average total fragment kinetic energy

The average total fragment kinetic energy as a function of the heavy fragment mass number, $\overline{\mathrm{TKE}}(A_H)$, shown in Fig. 2, is used in conjunction with the corresponding dispersion, $\sigma_{\mathrm{TKE}}(A_H)$, to construct the conditional probability distribution $Y(\mathrm{TKE}|A)$ as shown in Eq. (1). The experimental data sets used for those two quantities are listed in Table I.

Most of those data come from the same set of experiments already discussed above for the mass yields. We have added a 1% fully correlated (normalization) uncertainty and a 0.5% additional statistical uncertainty to all data sets. These are reasonable estimates based on the rather small spread of the data reported across the different experiments. (A 1% uncertainty on TKE corresponds to a 1.5- to 2-MeV absolute uncertainty.) Near symmetry and for very asymmetric divisions, we included additional uncertainties to account for the larger spread of the data resulting from the small number of fragments measured in those regions,

$$\delta y_i = 0.002 \times y_i \exp[(132 - A_i)/2], \quad A_i < 132, \quad (3)$$

$$\delta y_i = 0.001 \times y_i \exp[(A_i - 160)/4], \quad A_i > 160, \quad (4)$$

where y_i denotes $\overline{\mathrm{TKE}}(A_i)$ here.

Experimental data on the standard deviation of TKE as a function of the heavy fission fragment mass are shown in Fig. 3. Significant differences exist between those three data sets, originating from the same experimental group at different times. The most recent set by Göök et al. [18] is presumably the most accurate one, given the reported accuracy in mass and energy resolutions obtained in that experiment. The oldest data set [13] did not provide any uncertainties and the plotted error bars are statistical only.

We have added a 4% normalization uncertainty and an additional 1% statistical uncertainty for all data sets. The "floating" normalization allowed the least-squares fit to find
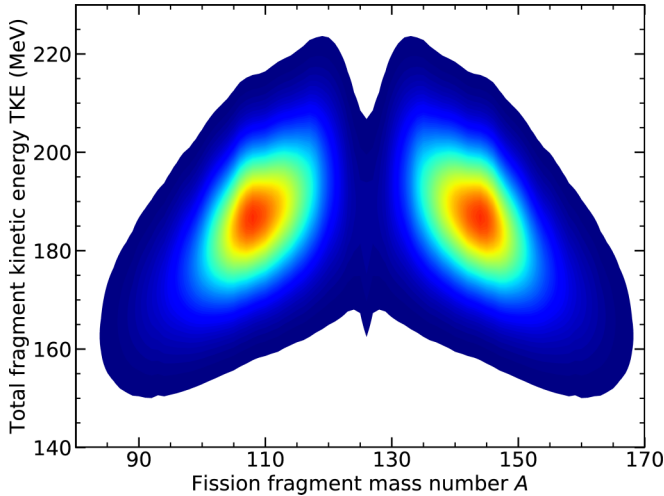
FIG. 4. Contour plot of the A-TKE projection, $Y(A, \mathrm{TKE})$, of one particular yield function $Y(A, Z, \mathrm{TKE})$ that was sampled randomly from the distribution of yield functions determined from our least-squares analysis of the experimental data, as described in the text.

a reasonable solution. As for $\overline{\mathrm{TKE}}(A_H)$, $\sigma_{\mathrm{TKE}}(A_H)$ grows less reliable as we move toward symmetric or very asymmetric divisions and we have similarly included additional uncertainties in those regions,

$$\delta y_i = 0.002 \times y_i \exp[(140 - A_i)/2], \quad A_i < 140, \qquad (5)$$

$$\delta y_i = 0.001 \times y_i \exp[(A_i - 165)/4], \quad A_i > 165, \qquad (6)$$

where y_i denotes $\sigma_{\mathrm{TKE}}(A_i)$ here.

C. Generalized least-squares fit to the data

The result of the least-squares fit to these experimental data is a best mean value as well as a covariance matrix that contains uncertainties and correlations for a range of fission fragment masses. In order to study the influence of different input yields on the results of the fission event simulations, we perform FREYA simulations for ensembles of (1000–15 000) yield functions sampled from the distribution of yield functions determined as described above. The sampling of the correlated yield functios was performed by using the method described in Appendix A.

As an illustration, Fig. 4 shows one particular (randomly selected) yield function $Y(A, Z, \mathrm{TKE})$ in the form of a contour plot of its projection onto the A-TKE plane.

III. EVENT SELECTION DETAILS

For the purpose of the present study, the fission event generator FREYA [2] has been modified so it takes the combined yield function $Y(A, Z, \mathrm{TKE})$ as input.

The initial nucleus has mass number A_0 and charge number Z_0. For each particular yield function, $Y(A, Z, \mathrm{TKE})$, the selection of the associated fission events is made as follows.

We assume that the joint yield function is normalized,

$$\sum_A \sum_Z \int d\mathrm{TKE}\, Y(A, Z, \mathrm{TKE}) = 1. \qquad (7)$$

First, the fragment mass A is selected from the probability distribution,

$$P_A(A) = \sum_Z \int d\mathrm{TKE}\, Y(A, Z, \mathrm{TKE}), \qquad (8)$$

which is normalized to unity, $\sum_A P_A(A) = 1$. Then the fragment charge Z is selected from the following conditional probability distribution:

$$P_Z(Z; A) = \int d\mathrm{TKE}\, Y(A, Z, \mathrm{TKE})/P_A(A), \qquad (9)$$

which is normalized to unity as well, $\sum_Z P_Z(Z; A) = 1$. Finally, the total kinetic energy TKE is selected from the conditional probability distribution,

$$P_{\mathrm{TKE}}(\mathrm{TKE}; A, Z) = Y(A, Z, \mathrm{TKE})/P_Z(Z; A), \qquad (10)$$

which is also normalized, $\int d\mathrm{TKE}\, P_{\mathrm{TKE}}(\mathrm{TKE}; A, Z) = 1$.

After the selection of (A, Z, TKE) has been made, the mass and charge numbers of the complementary fragment are obtained as $A' = A_0 - A$ and $Z' = Z_0 - Z$, respectively, and the total excitation energy is given by

$$E^*(A, Z, \mathrm{TKE}) = Q(A, Z) - \mathrm{TKE}, \qquad (11)$$

where $Q(A, Z) = M(A_0, Z_0) - M(A, Z) - M(A', Z')$ is the Q value for this particular division.

The quantity E^* plays a key role in determining the resulting neutron multiplicity. Because the mean neutron multiplicity is rather well measured experimentally, $\nu_0 \equiv \bar{\nu}_{\exp} = 3.756 \pm 0.4\%$ [22], and many applications require its calculated value to be fairly accurate, FREYA performs an adjustable TKE shift, $d\mathrm{TKE}$, to ensure that the calculated $\bar{\nu}$ is satisfactory. In the present study, we use $d\mathrm{TKE} = 1.15$ MeV which ensures that the overall mean neutron multiplicity reproduces the experimental value, $\prec \bar{\nu} \succ = \nu_0$.

The dinuclear rotational modes can then be populated by the usual FREYA procedure [23]. Finally, the remaining excitation energy E^*_{stat} should be divided between the two fragments. As in the standard FREYA, this is done in two steps: First, a tentative partitioning of E^*_{stat} is made statistically, yielding E'_L and E'_H. Subsequently, the light fragment is favored to a degree controlled by the FREYA parameter x, $E^*_L = x\, E'_L$ (implying $E^*_H = E^*_{\mathrm{stat}} - E^*_L$). However, the standard FREYA procedure samples E'_L and E'_H. From the canonical (i.e.,thermal) distribution in each fragment separately and then restores energy conservation by adjusting TKE as needed. But that procedure is not possible in the present study because the value of TKE is specified. The combined fragment excitation must be equal to the total amount available, E^*_{stat}, so the sampling of E'_L and E'_H is made microcanonically, as described in Appendix B.

IV. NEUTRON OBSERVABLES

We consider an ensemble of N yield functions, $\{Y^{(i)}(A, Z, \mathrm{TKE})\}$, $i = 1, \ldots, N$, sampled on the basis of
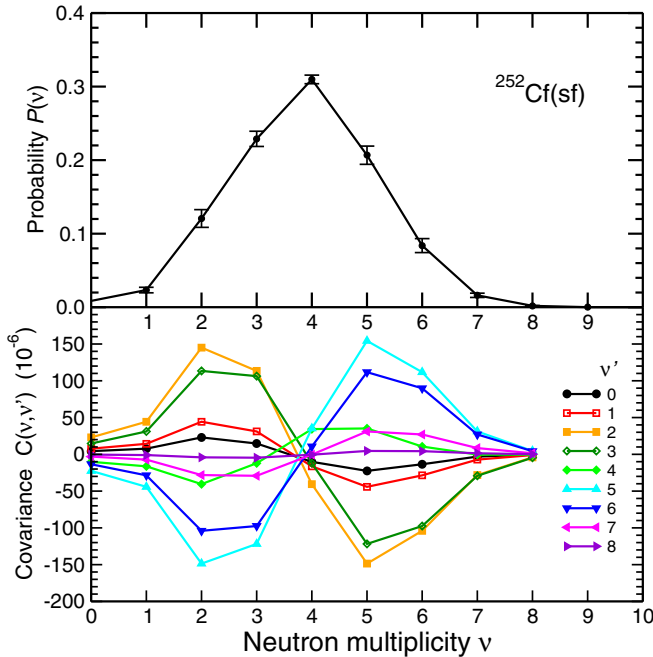
FIG. 5. The neutron multiplicity distribution $P_n(\nu)$ (top) and the elements of the neutron multiplicity covariance matrix $C_{nn}(\nu, \nu')$ shown as functions of ν for the various values of ν' (bottom), calculated for the ensemble of yield functions described in the text. The curves show the overall ensemble average values, while the error bars on $P_n(\nu)$ reflect the associated ensemble dispersions [see Eq. (14)].

the experimental data as described above, and we wish to extract the ensemble average of various neutron observables and the associated ensemble dispersions. As we will explain below, we may generally wish to give an individual weight to each particular yield function, W_i (with $\sum_i W_i = 1$), rather than always using $W_i = 1/N$.

The use of several thousand sampled yield functions ensures that the extracted quantities are well determined. Furthermore, the number of events generated for each yield function, K (usually $K = 10^6$), is sufficiently large to ensure that the associated statistical fluctuations of the considered observables are small in comparison with those reflecting the fact that we consider an entire ensemble of N different yield functions.

A. Neutron multiplicity

For a given yield function $Y^{(i)}(A, Z, TKE)$, the distribution function for the neutron multiplicity ν is denoted by $P_n^{(i)}(\nu)$, with $\sum_\nu P_n^{(i)}(\nu) = 1$. The ensemble-averaged multiplicity distribution is then given by

$$\prec P_n(\nu) \succ = \sum_{i=1}^{N} W_i P_n^{(i)}(\nu), \qquad (12)$$

and it is also normalized, $\sum_\nu \prec P_n(\nu) \succ = 1$. This quantity is shown in Fig. 5 (top) with error bars indicating the associated ensemble fluctuations $\sigma_{\bar{\nu}}$ [see Eq. (14) below].
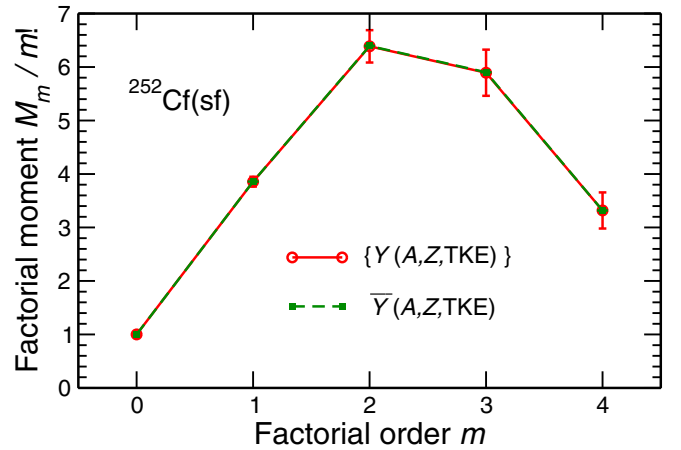
FIG. 6. Factorial moments of the neutron multiplicity distribution [see Eq. (15)], as obtained either from the sample of yield functions $\{Y^{(i)}(A, Z, TKE)\}$, with 10^6 events generated for each one (solid curve), or from reusing the average yield function $\overline{Y}(A, Z, TKE)$ equally many times (dashed curve). Each factorial moment $\mathcal{M}_m$ has been divided by $m!$ to compensate for the rapid growth with the order m.

The covariance matrix $\boldsymbol{C}_{nn} = \{C_{nn}(\nu, \nu')\}$ for the multiplicity distribution can also be extracted from the ensemble of multiplicity distributions $\{P_n^{(i)}(\nu)\}$,

$$C_{nn}(\nu, \nu') = \prec P_n(\nu)P_n(\nu') \succ - \prec P_n(\nu) \succ \prec P_n(\nu') \succ$$
$$= \sum_{i=1}^{N} W_i P_n^{(i)}(\nu) P_n^{(i)}(\nu') - \prec P_n(\nu) \succ \prec P_n(\nu') \succ . \qquad (13)$$

The elements $C_{nn}(\nu, \nu')$ are plotted in Fig. 5 (bottom) as functions of ν' for each value of ν. The pronounced anticorrelation between high and low multiplicity reflects the elementary fact that each multiplicity distribution is normalized to unity, so those that are above average for higher ν values must be below average for low ν values and vice versa.

The diagonal elements of $C_{nn}(\nu, \nu')$ are the variances of $P_n(\nu)$ (i.e., the variance of the $\bar{\nu}$ values obtained with the different yield functions),

$$\sigma_\nu^2 = C_{nn}(\nu, \nu) = \sum_{i=1}^{N} W_i \left[P_n^{(i)}(\nu) \right]^2 - (\prec P_n(\nu) \succ)^2 . \quad (14)$$

The associated ensemble dispersions σ_ν are shown as the error bars in Fig. 5 (top). Because of the above-mentioned anticorrelation, the different curves in Fig. 5 (bottom) all cross through zero near $\nu = \prec \bar{\nu} \succ$. As a result, $\sigma_{\nu=4}$ is particularly small.

The factorial moments of the neutron multiplicity distribution $P_n^{(i)}(\nu)$ are given by

$$\mathcal{M}_m^{(i)} \equiv \sum_\nu \nu(\nu - 1) \cdots (\nu - m + 1) P_n^{(i)}(\nu), \qquad (15)$$

so $\mathcal{M}_0^{(i)}$ is unity and $\mathcal{M}_1^{(i)}$ is the mean multiplicity $\bar{\nu}^{(i)}$. These are shown in Fig. 6 for orders $m = 0, 1, 2, 3, 4$, with the ensemble fluctuations indicated by the error bars. To illustrate the negligible magnitude of the statistical uncertainties arising
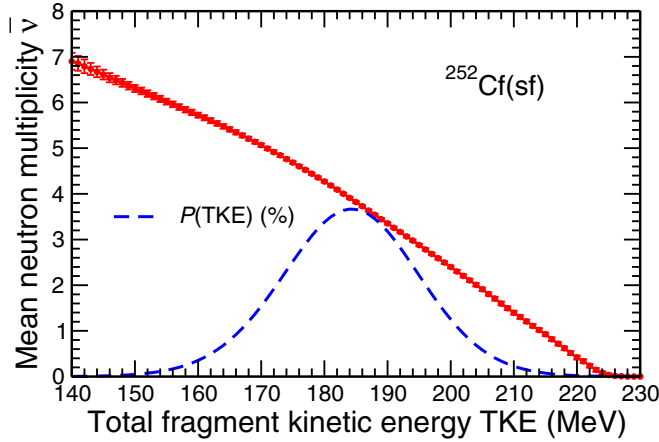
FIG. 7. The dependence of the mean neutron multiplicity $\bar{\nu}$ on TKE, the total kinetic energy of the fission fragments. Also shown is the overall distribution of TKE over the ensemble of yield functions (dashed curve).

from the finite number of events generated for each yield function, we also show the result of reusing the same (namely the average) yield function in which case there are no ensemble fluctuations so all fluctuations are statistical. These are seen to indeed be negligible in comparison with those arising from the use of an ensemble of different yield functions.

As already discussed in Sec. III, the neutron multiplicity is tightly correlated with the available excitation energy E^* which in turn is reated to the total fragment kinetic energy TKE by energy conservation. Consequently, the average neutron multiplicity $\bar{\nu}$ is strongly (anti)correlated with TKE, as illustrated in Fig. 7. This important feature will be further explored in Sec. V.

B. Neutron spectrum

For each particular (nonvanishing) neutron multiplicity ν, the associated spectral distribution is denoted by $\chi_n^{(\nu)}(\varepsilon)$; it is normalized to unity, $\int \chi_n^{(\nu)}(\varepsilon) \, d\varepsilon = 1$. The energy distribution of those neutrons may be written as

$$\left(\frac{d\nu}{d\varepsilon}\right)^{(\nu)} = \nu \, \chi_n^{(\nu)}(\varepsilon) \tag{16}$$

and is normalized to ν. The overall neutron energy distribution $d\nu/d\varepsilon$, which is normalized to the mean multiplicity $\bar{\nu}$, is then given by

$$\frac{d\nu}{d\varepsilon} = \sum_{\nu>0} \left(\frac{d\nu}{d\varepsilon}\right)^{(\nu)} P_n(\nu) = \bar{\nu} \, \chi_n(\varepsilon), \tag{17}$$

where $\chi_n(\varepsilon)$ is the overall spectral distribution of the emitted neutrons.

In the present study, we concentrate on the overall spectral distribution. For a given yield function $Y^{(i)}(A, Z, \mathrm{TKE})$, the resulting neutron energy distribution is denoted by $\chi_n^{(i)}(\varepsilon)$ and the ensemble-averaged neutron energy distributions is
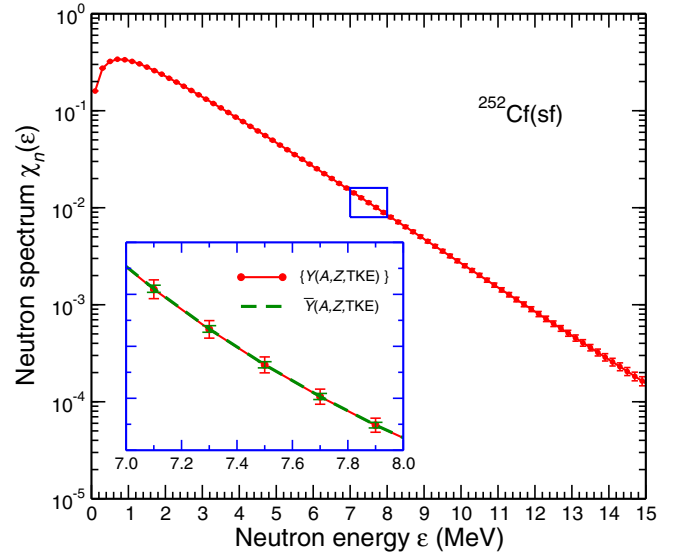
FIG. 8. The spectral distribution up to 15 MeV (logarithmic scale). The magnified (linear) view for $\varepsilon = 7$–8 MeV (insert) also shows the significantly smaller statistical uncertainties (wider error bars) arising from the 10^6 events generated for each yield function.

given by

$$\prec \chi_n(\varepsilon) \succ = \sum_{i=1}^{N} W_i \, \chi_n^{(i)}(\varepsilon), \tag{18}$$

and it is normalized to unity.

The spectral distribution of the evaporated neutrons, $\chi_n(\varepsilon)$, is approximately of Maxwellian form (with $T \approx 1.42$ MeV). With one million events, $\chi(E)$ can be sampled to a reasonable degree of accuracy out to ≈ 15 MeV. The effect of the uncertainty of the input yield function $Y(A, Z, \mathrm{TKE})$ on the spectral distribution of the evaporated neutrons is illustrated in Fig. 8. The magnified view for $\varepsilon = 7$–8 MeV shows the unimportance of the statistical uncertainties arising from the finite number of events generated for each yield function.

The energy-energy correlation function can also readily be extracted,

$$C_{nn}(\varepsilon, \varepsilon')$$
$$= \sum_{i=1}^{N} W_i \, \chi_n^{(i)}(\varepsilon) \, \chi_n^{(i)}(\varepsilon') - \prec \chi_n(\varepsilon) \succ \prec \chi_n(\varepsilon') \succ. \tag{19}$$

It is shown in Fig. 9 with the diagonal part subtracted to better bring out how two different energies are correlated. There is a significant positive correlation when both energies are below 2 MeV or so. This is the typical energy range of the evaporated neutrons and if one neutron is emitted with an energy in this range, there is a good chance that one or more additional neutrons are also emitted and that these are not very energetic. By contrast, the correlation is negative when one energy is low and the other is high, probably because the emission of an energetic neutron increases the likelihood that any additional neutron will not be energetic. When both energies are high there is hardly any correlation at all.
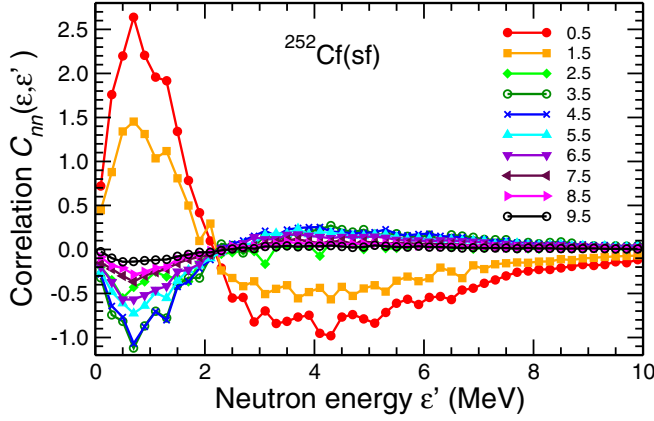
FIG. 9. The neutron energy-energy correlation function $C_{nn}(\varepsilon, \varepsilon')$ given in Eq. (19), with the diagonal term subtracted, shown as a function of ε' for specified values of ε as indicated (in MeV) for each curve.

C. Neutron-neutron angular correlations

A given event produces ν neutrons having the momenta $\boldsymbol{p}_j = p_j \hat{\boldsymbol{p}}_j$, $j = 1, \ldots, \nu$, where the emission directions are given by the unit vectors $\hat{\boldsymbol{p}}_j = (\sin \vartheta_j \cos \varphi_j, \sin \vartheta_j \sin \varphi_j, \cos \vartheta_j)$. The directional distribution of the neutrons is given by $P_n(\hat{\boldsymbol{p}})$ which is normalized to ν, the event multiplicity,

$$\int d^2 \hat{\boldsymbol{p}}\, P_n(\hat{\boldsymbol{p}}) = \int_{-1}^{+1} d \cos \vartheta \int_0^{2\pi} d\varphi\, P_n[\hat{\boldsymbol{p}}(\vartheta, \varphi)] = \nu. \quad (20)$$

while the joint probability for neutron emission into the two directions $\hat{\boldsymbol{p}}$ and $\hat{\boldsymbol{p}}'$ is denoted by $P_{nn}(\hat{\boldsymbol{p}}, \hat{\boldsymbol{p}}')$ which is normalized to $\nu(\nu - 1)$, twice the number of neutron pairs in the event.

For a sample of K events, each event k has directional distributions, $P_n^{(k)}(\hat{\boldsymbol{p}})$ and $P_{nn}^{(k)}(\hat{\boldsymbol{p}}, \hat{\boldsymbol{p}}')$. The overall angular distribution is then given by

$$\overline{P}_n(\hat{\boldsymbol{p}}) = \frac{1}{K} \sum_{k=1}^{K} P_n^{(k)}(\hat{\boldsymbol{p}}), \quad (21)$$

being normalized to the mean neutron multiplicity $\overline{\nu}$. Furthermore, the overall two-neutron directional distribution is

$$\overline{P}_{nn}(\hat{\boldsymbol{p}}, \hat{\boldsymbol{p}}') = \frac{1}{K} \sum_{k=1}^{K} P_{nn}^{(k)}(\hat{\boldsymbol{p}}, \hat{\boldsymbol{p}}'). \quad (22)$$

It is normalized to twice the mean number of neutron pairs in an event, $\langle \nu(\nu - 1) \rangle$. Obviously, only events that produce at least one neutron can contribute to $\overline{P}_n(\hat{\boldsymbol{p}})$ and only events producing at least two neutrons can contribute to $P_{nn}(\hat{\boldsymbol{p}}, \hat{\boldsymbol{p}}')$.

The cosine of the opening angle between the directions of two emitted neutrons 1 and 2 is determined by

$$\cos \theta(\hat{\boldsymbol{p}}_1, \hat{\boldsymbol{p}}_2) = \hat{\boldsymbol{p}}_1 \cdot \hat{\boldsymbol{p}}_2 = \sin \vartheta_1 \sin \vartheta_2 \cos(\varphi_1 - \varphi_2). \quad (23)$$

Consequently, the distribution of this quantity can be obtained as

$$\overline{P}_{nn}(\cos \theta_{12})$$
$$= \int d^2 \hat{\boldsymbol{p}} \int d^2 \hat{\boldsymbol{p}}'\, \overline{P}_{nn}(\hat{\boldsymbol{p}}, \hat{\boldsymbol{p}}')\, \delta[\cos \theta(\hat{\boldsymbol{p}}, \hat{\boldsymbol{p}}') - \cos \theta_{12}],$$
$$(24)$$
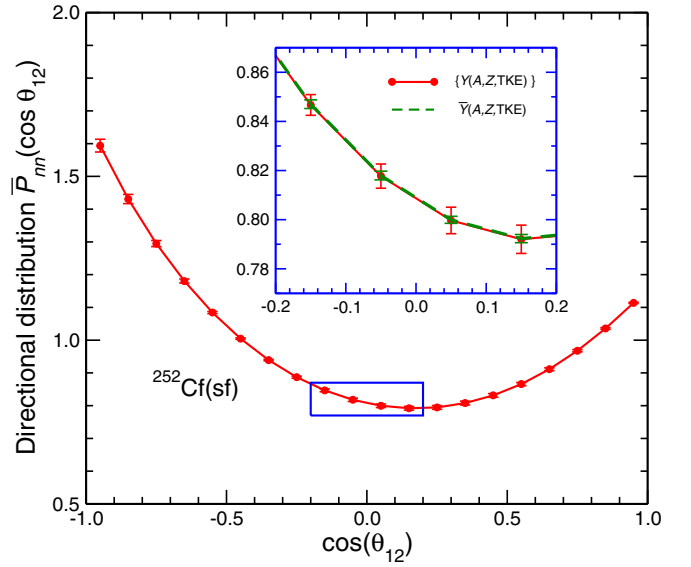
FIG. 10. The distribution $\overline{P}_{nn}(\cos \theta_{12})$, where θ_{12} is the specified opening angle between the directions of two neutrons in an event. The main panel covers the entire angular range, $0° \leqslant \theta_{12} \leqslant 180°$, while the insert shows the central region, $\theta_{12} \approx 90°$, and also displays the significantly smaller statistical uncertainties (wider error bars) obtained from always using the same yield function (see text).

with the normalization $\int d \cos \theta\, \overline{P}_{nn}(\cos \theta) = \langle \nu(\nu - 1) \rangle$.

Because the above discussion pertains to a particular given yield function $Y^{(i)}(A, Z, \text{TKE})$ it may be labeled by the index i, $\overline{P}_{nn}^{(i)}(\cos \theta_{12})$. If we repeat the procedure for an ensemble of N yield functions, then the resulting ensemble average directional distribution function is

$$\prec \overline{P}_{nn}(\cos \theta_{12}) \succ = \sum_{i=1}^{N} W_i \overline{P}_{nn}^{(i)}(\cos \theta_{12}). \quad (25)$$

The associated ensemble variance is

$$\prec \overline{P}_{nn}(\cos \theta_{12})^2 \succ - (\prec \overline{P}_{nn}(\cos \theta_{12}) \succ)^2$$
$$= \sum_{i=1}^{N} W_i \left[\overline{P}_{nn}^{(i)}(\cos \theta_{12}) \right]^2 - \left[\sum_{i=1}^{N} W_i \overline{P}_{nn}^{(i)}(\cos \theta_{12}) \right]^2. \quad (26)$$

The distribution (25) of $\cos \theta_{12}$ is shown in Fig. 10 over both the entire range of the opening angle $\cos \theta_{12}$ and for a limited region around $\theta_{12} = 90°$, with the dispersions from Eq. (26) shown as error bars.

V. RELATION BETWEEN ν AND TKE

In the preceding section, we have examined how the experimental uncertainty in the yield function $Y(A, Z, \text{TKE})$ affects a variety of neutron observables. We start this section by considering the distribution of the mean neutron multiplicities $\{\overline{\nu}_i\}$ resulting from the ensemble of yield functions, $\{Y^{(i)}(A, Z, \text{TKE})\}$. As illustrated in Fig. 11, $\overline{\nu}$ has an approximately Gaussian distribution with a mean value very close to the experimentally observed value, $\nu_0 = 3.756$, and a dispersion given by $\sigma_0 = 0.093$.
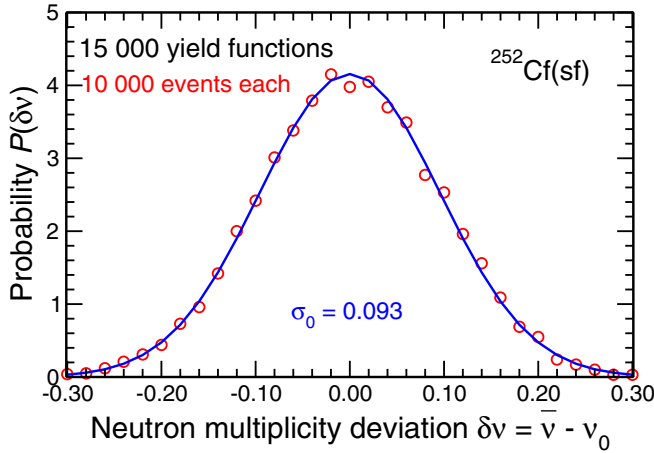
FIG. 11. The distribution of the deviation $\delta\nu$ of the resulting mean neutron multiplicity, $\bar{\nu}$, from the observed value, ν_0 (circles), together with the corresponding Gaussian function having the same mean and dispersion.

As noted above (see Fig. 7), there is a pronounced anticorrelation between the neutron multiplicity and the total fragment kinetic energy. This relationship is brought out visually in Fig. 12, which displays a scatter plot of the values of $(\bar{\nu}^{(i)}, \overline{\mathrm{TKE}}^{(i)})$ obtained for the ensemble of 15 000 yield functions sampled from the distribution $\mathcal{P}[Y(A, Z, \mathrm{TKE})]$ constructed from our χ^2 analysis of the experimental data (see Sec. II). Clearly, yield functions that lead to large/small mean neutron multiplicities also lead to small/large mean fragment kinetic energies.

Figure 13 shows a similar scatter plot of the corresponding ensemble dispersions in $\bar{\nu}$ and $\overline{\mathrm{TKE}}$. It is seen that large/small fluctuations in neutron multiplicity is associated with large/small dispersions in TKE.

It is possible to quantify the correlation between $\bar{\nu}$ and $\overline{\mathrm{TKE}}$ by assuming that the joint distribution of these two observables has a Gaussian form characterized by the 2×2
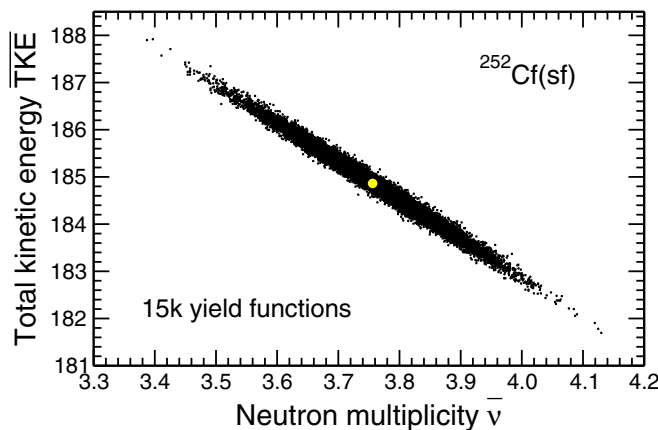
FIG. 12. A scatter plot of the mean neutron multiplicity, $\bar{\nu}$, and the mean total fragment kinetic energy, $\overline{\mathrm{TKE}}$, obtained for each of the 15 000 sampled yield functions. The overall average is indicated by the central dot.
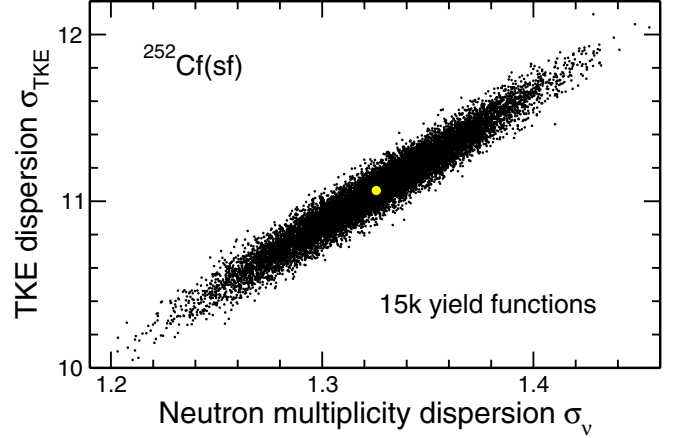
FIG. 13. A scatter plot of the dispersion of the neutron multiplicity, σ_ν, and the dispersion of the total fragment kinetic energy, σ_{TKE}, obtained for each of the 15 000 sampled yield functions. The overall average is indicated by the central dot.

covariance tensor $\boldsymbol{\sigma}$,

$$\boldsymbol{\sigma} = \begin{pmatrix} \sigma_{\nu\nu} & \sigma_{\nu K} \\ \sigma_{\nu K} & \sigma_{KK} \end{pmatrix}. \tag{27}$$

Its elements are given by

$$\sigma_{\nu\nu} = \sigma_\nu^2 = \prec \delta\nu^2 \succ, \tag{28}$$

$$\sigma_{\nu K} = \prec \delta\nu\,\delta K \succ, \tag{29}$$

$$\sigma_{KK} = \sigma_K^2 = \prec \delta K^2 \succ, \tag{30}$$

where we have introduced the deviations $\delta\nu \equiv \bar{\nu} - \prec \bar{\nu} \succ$ and $\delta K \equiv \overline{\mathrm{TKE}} - \prec \overline{\mathrm{TKE}} \succ$ for notational convenience.

The determinant of $\boldsymbol{\sigma}$ is given by $D = \sigma_\nu^2 \sigma_K^2 - \sigma_{\nu K}^2$ and its inverse tensor $\boldsymbol{m}$ has the following elements,

$$m_{\nu\nu} = m_\nu^2 = \sigma_K^2/D, \tag{31}$$

$$m_{\nu K} = -\sigma_{\nu K}/D, \tag{32}$$

$$m_{KK} = m_K^2 = \sigma_\nu^2/D. \tag{33}$$

We thus assume that the (normalized) joint distribution is given by

$$P(\bar{\nu}, \overline{\mathrm{TKE}}) = \frac{1}{2\pi\sqrt{D}}\, e^{-\frac{1}{2}[m_\nu^2\delta\nu^2 + 2m_{\nu K}\delta\nu\delta K + m_K^2\delta K^2]}. \tag{34}$$

From the joint distribution we can recover the individual distributions by projection,

$$P_n(\bar{\nu}) = \int P(\bar{\nu}, \overline{\mathrm{TKE}})\, d\overline{\mathrm{TKE}} = \frac{1}{\sqrt{2\pi}\,\sigma_\nu} e^{-\delta_\nu^2/2\sigma_\nu^2}, \tag{35}$$

$$P(\overline{\mathrm{TKE}}) = \int P(\bar{\nu}, \overline{\mathrm{TKE}})\, d\bar{\nu} = \frac{1}{\sqrt{2\pi}\,\sigma_K} e^{-\delta_K^2/2\sigma_K^2}. \tag{36}$$

The $\bar{\nu}$ distribution, $P_n(\bar{\nu})$, was displayed in Fig. 11. The spread in the calculated $\bar{\bar{\nu}}$ values, $\sigma_\nu = 0.093$, is about 2.5% of the mean multiplicity, $\nu_0 = 3.756$. This is more than a factor of six larger than the approximately 4 per mille uncertainty on the measured multiplicity, namely $\sigma_0 = 0.015$ [22]. We therefore wish to introduce a bias on each sampled yield function

so that those yield functions that produce mean multiplicities close to the observed value are given more credibility than those leading to significant deviations, even though all the yield functions have been sampled in accordance with the experimental uncertainties reported on the measured A, Z, and TKE.

Thus, for a given yield function $Y^{(i)}(A, Z, \text{TKE})$, we employ a $\bar{\nu}$-dependent weight,

$$W_i \sim \exp\left[-(\bar{\nu}^{(i)} - \nu_0)^2 / 2\sigma_0^2\right], \qquad (37)$$

rather than the constant weight $W_i = 1/N$ used above.

With the Gaussian approximation introduced in Eq. (34), it is straightforward to determine the effect of such a weighting. The resulting biased distribution is given by

$$\tilde{P}(\bar{\nu}, \overline{\text{TKE}}) = W(\delta\nu) P(\bar{\nu}, \overline{\text{TKE}}), \qquad (38)$$

where $P(\bar{\nu}, \overline{\text{TKE}})$ is the unbiased distribution given in Eq. (34) and the bias factor is the weight in Eq. (37), $W(\delta\nu) \sim \exp(-\delta\nu^2 / 2\sigma_0^2)$.

The resulting biased $\overline{\text{TKE}}$ distribution can then be obtained by integrating $\tilde{P}(\bar{\nu}, \overline{\text{TKE}})$ over $\bar{\nu}$. This can be accomplished by elementary means (see Appendix C), yielding $\tilde{P}(\overline{\text{TKE}}) \sim \exp(-\delta K^2 / 2\tilde{\sigma}_K^2)$ where the biased variance is given by

$$\tilde{\sigma}_K^2 = \sigma_K^2 - \frac{\sigma_{\nu K}^2}{\sigma_\nu^2 + \sigma_0^2}. \qquad (39)$$

The limit of a large bias width, $\sigma_0 \to \infty$, corresponds to not imposing any bias at all (all weights are the same) and, accordingly, it yields $\tilde{\sigma}_K^2 \to \sigma_K^2$. In the opposite limit of a very narrow bias, $\sigma_0 \to 0$, only values of $\bar{\nu}$ very close to ν_0 are accepted, which corresponds to cutting the two-dimensional distribution (see Fig. 12) along the line $\delta\nu = 0$, yielding $\tilde{\sigma}_K^2 \to D/\sigma_\nu^2 = 1/m_K^2$. Thus the largest possible value of $\tilde{\sigma}_K(\sigma_0)$ is the unbiased width σ_K, while the smallest achievable value of $\tilde{\sigma}_K(\sigma_0)$ is $\tilde{\sigma}_K(0) = 1/m_K$. This behavior is illustrated in Fig. 14 from which it is apparent that the Gaussian approximation provides a very accurate representation of the actual numerical results.

In the present investigation, we wish to use a bias width that is equal to the experimental *rms* uncertainty on $\bar{\nu}$ which is about 15.4% of the width obtained for the unbiased ensemble of yield functions, as shown in Fig. 11. This leads to a reduction of the width of $\overline{\text{TKE}}$ from about 780 keV to about 135 keV. Thus σ_{TKE} is reduced to about 17.2% of its unbiased value when the multiplicity-dependent bias is applied. The fact that σ_ν and σ_{TKE} are reduced by approximately the same factor is a reflection of the high degree of correlation between the two observables (see Fig. 12), as is signalled by the very small value of the determinant $D = |\sigma|$.

VI. SENSITIVITY TO FREYA PARAMETERS

The studies in this section are carried out with the current standard version of FREYA. The code contains a number of parameters that have been adjusted to reproduce various aspects of the experimental data for each particular case of interest, presently $^{252}\text{Cf(sf)}$. As a result, the calculated neutron-related observables tend to be in quite good agreement with the
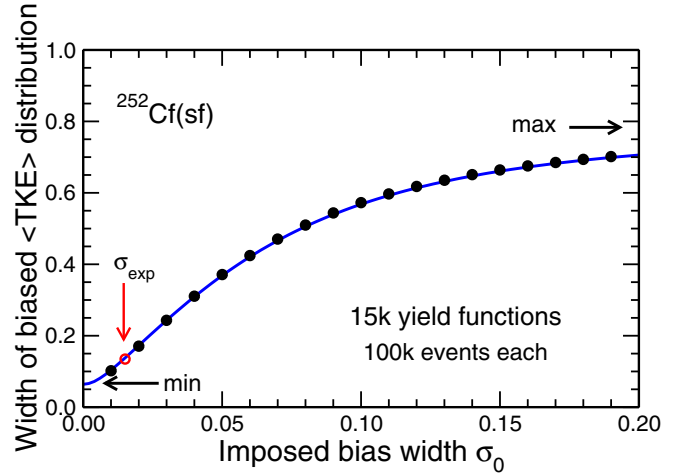
FIG. 14. The width of the $\overline{\text{TKE}}$ distribution as a function of the specified bias width σ_0 in the weight $W \sim \exp(-\delta\nu^2 / 2\sigma_0^2)$ of the individual yield functions $Y(A, Z, \text{TKE})$, as extracted for specific values of σ_0 (dots) or as given by the analytical expression (39) (curve). The maximum value (indicated by "max") is obtained for $\sigma_0 \to \infty$ and results when all yield functions are weighted equally, while the minimum value (indicated by "min") is obtained for $\sigma_0 \to 0$ and is the width of the distribution resulting from making a cut at $\delta\nu = 0$, i.e.,, $\tilde{P}(\delta K) \sim P(\delta\nu = 0, \delta K)$. The value obtained when using the experimental uncertainty on $\bar{\nu}$ is indicated (circle). The calculations sampled 100 000 fission events from each of 15 000 yield functions for $^{252}\text{Cf(sf)}$.

experimenal data. A notable exception is the mass dependence of the average neutron multiplicity, $\bar{\nu}(A)$, shown in Fig. 15.

A. Excitation energy partitioning

The function $\bar{\nu}(A)$ is sensitive to the FREYA parameter x which controls the division of the available excitation energy
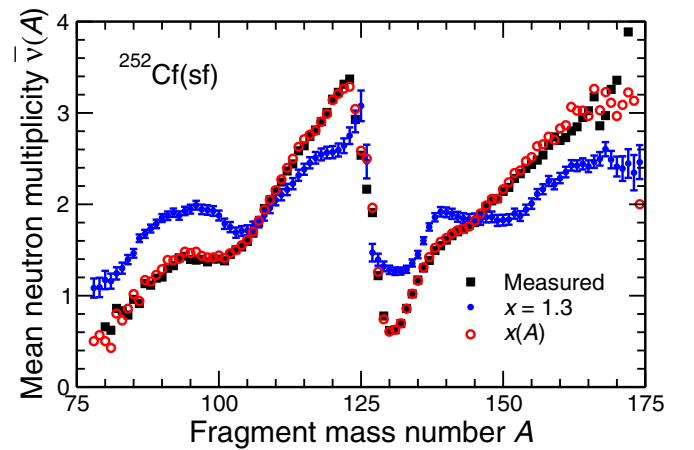
FIG. 15. The mean neutron multiplicity as a function of the mass number of the primary fragment, $\bar{\nu}(A)$, as obtained with FREYA when using either the standard constant value $x = 1.3$ or the mass-dependent value $x(A)$ shown in Fig. 16. Also shown is the least-squares fit to five sets of experimental data [17,24–27] used to determine $x(A)$.
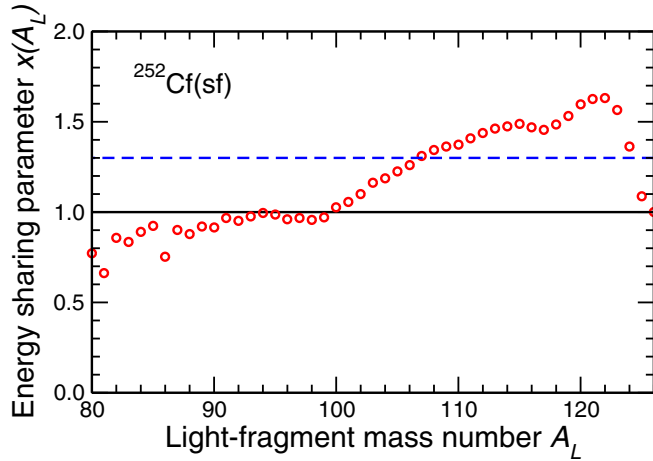
FIG. 16. The extracted mass-dependent energy sharing parameter $x(A_L)$ obtained by matching the calculated light-to-heavy neutron multiplicity ratio $\bar{\nu}_L/\bar{\nu}_H$ to the data for each mass split. Also shown is the standard (constant) value $x = 1.3$ (dashed line).

FIG. 17. The mean energy of the evaporated neutrons (in the frame of the emitting nucleus) as a function of the primary fragment mass number, $\bar{\varepsilon}(A)$, as obtained with the standard FREYA version that uses a constant value, $x = 1.3$, and with the modified version using the A-dependent value $x(A)$ shown in Fig. 16.

between the two nacscent fragments. With only a single parameter, the overall appearance of $\bar{\nu}(A)$ can be reasonably reproduced, but not its detailed behavior which is sensitive to specific structure effects in the fragments. In order to elucidate the importance of this shortcoming, we have introduced a mass-dependent x parameter, $x(A)$, determined as follows.

First, we make a series of FREYA runs with successively increasing values of x and tabulate the resulting multiplicity ratios $r(A_L; x) \equiv \bar{\nu}(A_L; x)/\bar{\nu}(A_H; x)$. Then, for each light-fragment mass number A_L, we determine (by interpolation) the x value that would give a multiplicity ratio equaling the experimental one, thus obtaining x for that fragmentation, $x(A_L)$. When FREYA is run with this $x(A_L)$ rather than a single constant x value, the resulting $\bar{\nu}(A)$ reproduces the data well. The relatively small local deviations are due to the fact that matching the multiplicity ratio $\bar{\nu}_L/\bar{\nu}_L$ does not ensure a perfect match of the two multiplicities $\bar{\nu}_L$ and $\bar{\nu}_R$ separately. The extracted function $x(A)$ is displayed in Fig. 16.

We note that the fission codes CGMF [3] and FIFRELIN [4] were developed with a mass-dependent energy sharing prescription, equivalent to the use of $x(A)$ in FREYA. If those codes were to use a mass-independent energy sharing prescription, then their results for the fragment yields [28,29] would be quite similar to those obtained with the standard FREYA.

In order to illustrate the effect of replacing a constant x by $x(A)$, in Fig. 17 we show the average kinetic energy of the evaporated neutrons as a function of the primary fragment mass number, $\bar{E}(A)$. The deviations of the constant-x results from the variable-x results for $\bar{E}(A)$ resemble those for $\bar{\nu}(A)$ because a fragment that is given more excitation energy tends to not only evaporate more neutrons but also make them more energetic. But a constant x leads to too high neutron energies for the lightest fragments (and, correspondingly, too low neutron energies for the heaviest fragments) and the sawtooth drop before the doubly closed shell at $A = 132$ is both too abrupt and too small.
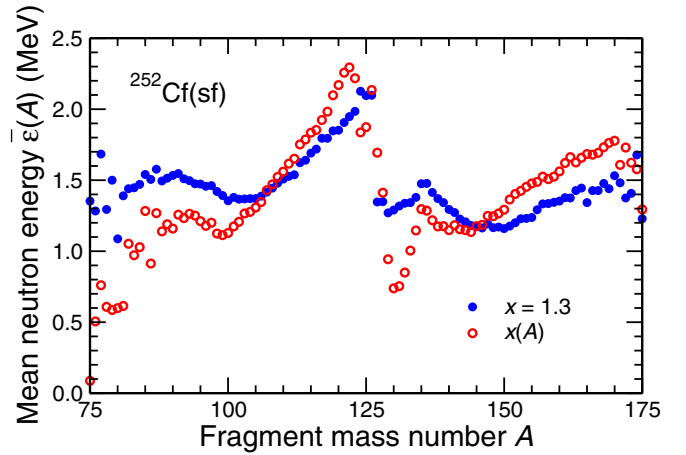
Nevertheless, even though $\bar{E}(A)$ changes significantly when going from a constant x to $x(A)$, the corresponding neutron spectra are almost identical within statistics. That is because most of the differences in $\bar{E}(A)$ and $\bar{\nu}(A)$ occur where the yields are small, either the tails or in the dip at symmetry, while the average neutron energies are similar near the average light and heavy fragment masses, $A_L \approx 110$ and $A_H \approx 140$. However, the spectra would also differ if only a limited A range were considered, for example $A < 110$.

Furthermore, we consider how the introduction of $x(A)$ affects the angular correlation between the neutrons. Figure 18 shows the distribution of the relative emission angle for two different minimum neutron energies: 0.4 MeV and 1.2 MeV. While the shapes appear quite similar at first glance, there is a small tilt toward large angular separations when a fixed x is replaced by $x(A)$, with a corresponding enhancement for neutrons emitted in similar directions. The difference between the two can be quantified by the ratio of the values at 180° and 0°. For fixed x, this ratio is 1.46 for $E > 0.4$ MeV and 1.44 for $E > 1.2$ MeV, while using $x(A)$ yields 1.37 and 1.31, respectively. Thus the effect on the angular correlation is more pronounced for higher-energy neutrons.

The sensitivity of the nucleon-nucleon angular correlation to other FREYA parameters was discussed in Ref. [23].

B. Other FREYA parameters

There are three other FREYA parameters relevant to the present study and we discuss them in turn below. For a discussion of parameter optimization in FREYA for spontaneous fission, see Ref. [30].

The parameter c adjusts the width of the variance of the statistical fragment excitation energy, because the idealized Gaussian form of the energy distribution is often truncated due to the limited energy available; otherwise, the resulting energy distribution would become too narrow. The optimized value of c varies significantly from case to case; for the present case,
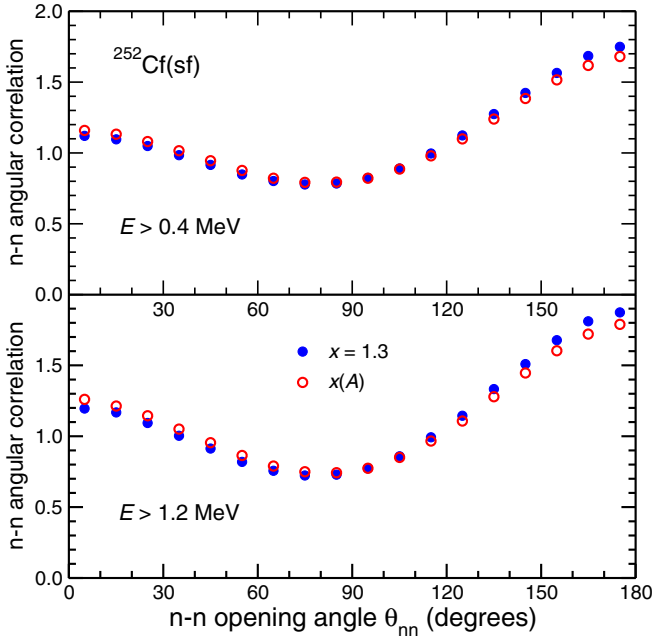
FIG. 18. The effect of $x(A)$ on the angular correlation between the neutrons. The distribution $\bar{P}_{nn}(\cos\theta_{12})$ [see Eq. (25)] as obtained with the standard FREYA version that uses a constant value $x = 1.3$ and with the modified version using the A-dependent value $x(A)$ shown in Fig. 16, for two different values of the minimum neutron energy accepted, either 0.4 MeV (top) or 1.2 MeV (bottom).

^{252}Cf(sf), it is $c = 1.19 \pm 0.36$ [30]. The neutron multiplicity distribution $P_n(\nu)$ is the only neutron observable having a noticeable sensitivity to c. For example, increasing c from 1 to 1.5 decreases $\bar{\nu}$ by 1.5%. But, if a good reproduction of the measured multiplicity distribution is to be maintained, other parameter adjustments would have to also be made, resulting in a very small net effect on $P_n(\nu)$ and its factorial moments $\mathcal{M}_m$ (including in particular $\bar{\nu} = \mathcal{M}_1$ whose range is dictated by experiment to be rather tight).

The FREYA parameter c_S controls the typical magnitude of the fragment angular momenta and it therefore affects the balance between neutron and photon emission. If c_S is increased, then the fragments will rotate more and, consequently, more photons will eventually be emitted (for a discussion of how c_S affects the photon observables, see Ref. [31]). At the same time, the increased rotational energy will leave less energy for statistical excitation of the primary fragments and thus there will be fewer neutrons evaporated and they will tend to be less energetic. For example, as discussed in Ref. [31], if all other parameters are kept unchanged, the average neutron multiplicity can decrease by as much as 12% if c_S is increased from 0.2 to 2.0. But such a wide range is unrealistic, as the range of reasonable c_S values is constrained by the measured photon multiplicity. The optimized parameter value does not depend much on the specific case and it is $c_S = 0.875 \pm 0.020$ for ^{252}Cf(sf) [30]. If c_S is varied within the resulting 1-σ range, then $\bar{\nu}$ changes by 0.34%.

Finally, the neutron multiplicity can depend on the parameter e_0 which scales the Fermi-gas nuclear level density

parameter, $a_A = A/e_0$. For a given fragment excitation energy, an increase of e_0 increases the fragment temperature. Consequently, the neutron spectrum hardens and the neutron multiplicity decreases. While the dependence of $\bar{\nu}$ on e_0 alone is effectively linear, e_0 is constrained by other parameter values that are optimized to data, including the prompt fission neutron spectrum. As a result, while the neutron spectrum and multiplicity depend on all the parameters, including e_0, the other neutron observables are not sensitive to e_0. The optimized value is $e_0 = 10.43 \pm 1.09/\text{MeV}$ [30]. Within this relatively large tolerance, the value of e_0 can be regarded as being universal, i.e., it has the same value for all fission fragments considered. Although changing e_0 within its range of uncertainty can change $\bar{\nu}$ by up to 2.7% and the average neutron energy by 7%, the constraints placed on the allowed range of $\bar{\nu}$ through optimization of the other parameters preclude such large changes.

Thus, while independent variations of a single parameter can produce somewhat significant changes in the neutron observables, including $\bar{\nu}$, such parameter modifications are not realistic due to the significant couplings between the different parameters resulting from the optimization procedure.

VII. CONCLUDING REMARKS

In this investigation, we have explored the sensitivity of important neutron observables produced by the fission simulation code FREYA for ^{252}Cf(sf) to various model inputs, primarily the specified yield function $Y(A, Z, \text{TKE})$ but also the intrinsic model parameters.

First, we compiled the available experimental data on the mass-dependent fragment yields, $Y(A)$, the mass-dependent average total fragment kinetic energy, $\overline{\text{TKE}}(A_H)$, and the associated TKE dispersion, $\sigma_{\text{TKE}}(A_H)$. Assuming that the TKE distribution has a Gaussian form for each A and invoking also the Wahl systematics for the charge distributions, we performed a χ^2 fit to obtain the most probably three-dimensional yield function $\bar{Y}(A, Z, \text{TKE})$. This procedure also yielded the associated covariance tensor for the probability distribution of possible yield functions, $\mathcal{P}[Y(A, Z, \text{TKE})]$, which in turn allowed us to generate an entire ensemble of possible yield functions. The application of FREYA for each such possible yield function then produces corresponding ensembles of observables whose variations reflect their sensitivity to the uncertainty in the experimental data.

We found that the neutron multiplicity distribution, $P_n(\nu)$, the neutron spectral shape, $\chi_n(E)$, and the neutron-neutron directional distribution, $P_{nn}(\cos\theta_{12})$, exhibited almost negligible sensitivity to the uncertainty in the specified yield function $Y(A, Z, \text{TKE})$.

Furthermore, we particularly studied the pronounced anticorrelation between the average total kinetic energy $\overline{\text{TKE}}$ and the average neutron multiplicity $\bar{\nu}$ which can be used to predict or reduce the uncertainty on one observable if the other one is known with sufficient accuracy. Under ideal circumstances, when the model is perfect and its parameters fixed, we have estimated that the evaluated uncertainty of $\bar{\nu}$ of 0.4% implies a standard deviation of 135 keV for $\overline{\text{TKE}}$, a significant reduction compared to the current experimental

uncertainty of nearly 1 MeV. Uncertainties in the model parameters, although constrained by complementary fission data, e.g.,photon multiplicity, will increase this estimate somewhat. Various approximations in the model itself and its implicit input, e.g., level density, also contribute to a higher estimate for the uncertainty on $\overline{\text{TKE}}$. It is difficult to quantify the final uncertainty precisely without further extending the present work to encompass all the input parameters entering in such calculations. However, it is clear that $\overline{\nu}$ imposes the most severe constraint on $\overline{\text{TKE}}$ and that other variations would have reltivelhy minor effects.

Finally, we determined the sensitivity of the neutron observables to variations in the intrinsic FREYA parameters. We have particularly studied the effect of replacing the default mass-independent division of the available excitation energy, governed by the parameter x, by a mass-dependent division governed by the function $x(A)$ determined from the measured $\overline{\nu}(A)$, similar to the prescriptions used in other codes [3,4]. While such a refinement has a significant effect on the mass-dependence of the average neutron multiplicity and the average neutron energy, the effect on the neutron-neutron angular correlations is small.

The present study shows the importance of developing a consistent theoretical model of nuclear fission that can predict a large variety of observables simultaneously. The intrinsic correlations that exist among those observables provide a powerful tool for constraining the fission models and their input parameters, leading to a more realistic and consistent description than what can be obtained with observable-specific models that aim to describe only parts of the fission data, such as the average neutron spectrum alone. Importantly, this type of analysis can be extended to other observables as well, such as those involving the fragment directions or the photons.

ACKNOWLEDGMENTS

APPENDIX A: SAMPLING OF YIELD FUNCTIONS

Each of the observables $Y(A)$, $\overline{\text{TKE}}(A)$, and $\sigma_{\text{TKE}}(A)$ can be regarded as an N-dimensional vector function $\boldsymbol{q} = \{q_i\}$, where $i = 1, \ldots, N$ represents the N possible values of the fragment mass number A. The analysis of the experimental data provides the mean value of the observable, $\overline{\boldsymbol{q}} = \{\bar{q}_i\} = \{\langle q_i \rangle\}$, as well as the associated covariance matrix, $\boldsymbol{C} = \{C_{ij}\} = \{\langle (q_i - \bar{q}_i)(q_j - \bar{q}_j) \rangle\}$. We assume that the distribution $\mathcal{P}[\boldsymbol{q}]$ of the actual function q is given by the corresponding multivariate N-dimensional Gaussian distribution,

$$\mathcal{P}[\boldsymbol{q}] = (2\pi)^{-\frac{N}{2}} |\boldsymbol{C}|^{-\frac{1}{2}} e^{-\frac{1}{2}(\boldsymbol{q}-\overline{\boldsymbol{q}})\cdot\boldsymbol{C}^{-1}\cdot(\boldsymbol{q}-\overline{\boldsymbol{q}})}, \quad (A1)$$

where $|\boldsymbol{C}|$ denotes the determinant of C.

In order to sample q, we first diagonalize the covariance matrix, $\boldsymbol{U}^{\dagger} \cdot \boldsymbol{C} \cdot \boldsymbol{U} = \{\lambda_i \delta_{ij}\}$, where λ_i are the N eigenvalues of C. (These are all positive because $\boldsymbol{C}$ is positive definite.) The corresponding eigenvectors, $\boldsymbol{u}_i = (u_{1i}, u_{2i}, \ldots, u_{Ni})$, are the elements of the rotation matrix $\boldsymbol{U} = \{u_{ij}\}$. A sampled function q can then be obtained as

$$\boldsymbol{q} = \overline{\boldsymbol{q}} + \boldsymbol{U} \cdot \boldsymbol{\epsilon}: \quad q_i = \bar{q}_i + \sum_{j=1}^{N} u_{ij}\epsilon_j, \quad (A2)$$

where the elements in the vector $\boldsymbol{\epsilon} = \{\epsilon_i\}$ have been sampled from the following probability distributions:

$$P_i(\epsilon_i) = \frac{1}{\sqrt{2\pi\lambda_i}} e^{-\epsilon_i^2/2\lambda_i}, \quad (A3)$$

respectively, so $\langle \epsilon_i \rangle = 0$ and $\langle \epsilon_i \epsilon_j \rangle = \lambda_i \delta_{ij}$.

It is elementary to show that an ensemble of functions $\boldsymbol{q} = \{q_i\}$ sampled according to the above procedure indeed has the desired first and second moments, $\langle q_i \rangle = \bar{q}_i$ and $\langle (q_i - \bar{q}_i)(q_j - \bar{q}_j) \rangle = C_{ij}$.

APPENDIX B: MICROCANONICAL ENERGY DIVISION

The total statistical excitation energy ε is partitioned between the two fragments, $\varepsilon = \varepsilon_L + \varepsilon_H$, in accordance with the appropriate microcanonical distribution. Thus the probability for the light fragment to acquire the excitation energy ε_L is given by

$$P_L(\varepsilon_L) \sim \rho_L(\varepsilon_L)\,\rho_H(\varepsilon - \varepsilon_H), \quad (B1)$$

where $\rho_f(\varepsilon_f)$ is the density of states in fragment $f = L, H$. The most probable energy division occurs when the derivative vanishes, $dP_L(\varepsilon_L)/d\varepsilon_L = 0$, leading to the condition $\beta_L(\varepsilon_L) = \beta_H(\varepsilon - \varepsilon_L)$, where $\beta_f(\varepsilon_f) \equiv d\ln\rho_f(\varepsilon_f)/d\varepsilon_f = 1/T_f(\varepsilon_f)$ is the inverse of the temperature of fragment f. Thus the most probable division occurs when the two fragment temperatures are equal, $T_L = T_H$.

Using the simple macroscopic Fermi-gas level density, $\rho_f(\varepsilon_f) \sim \exp(2\sqrt{a_f\varepsilon_f})$, where $a_f = A_f/e_0$ is the level-density parameter for fragment f, we have $\ln\rho_f(\varepsilon_f) = 2\sqrt{a_f\varepsilon_f}$, hence $T_f = \sqrt{\varepsilon_f/a_f}$. The most probable excitations, $\underline{\varepsilon}_f$, are then proportional to the respective level-density parameters, $\underline{\varepsilon}_f = a_f T^2$, where $T = \sqrt{\varepsilon/(a_L + a_H)}$ is the common temperature.

The variance of $P(\varepsilon_L)$ is equal to the variance of $P(\varepsilon_H)$ (because $\varepsilon_L + \varepsilon_H$ remains constant) and it is given (approximately) by

$$\sigma_f^2 \approx -\left[\frac{d^2 \ln P(\varepsilon_f)}{d\varepsilon_f^2}\right]_{\varepsilon_f=\underline{\varepsilon}_f}^{-1} = \frac{2T\varepsilon\,a_L a_H}{(a_L + a_H)^2} = 2T\frac{\varepsilon_L\varepsilon_H}{\varepsilon}. \quad (B2)$$

The canonical variances used previously in FREYA are given by $\tilde{\sigma}_f^2 \approx 2T\underline{\varepsilon}_f$, so the effect of the microcanonical constraint is to replace the actual mean fragment excitation $\underline{\varepsilon}_f$ by the reduced value $\underline{\varepsilon}_L\underline{\varepsilon}_H/\varepsilon$. Thus the microcanonical variance is smaller than either of the individual canonical variances. As one would expect, the canonical variance is approached, $\sigma_L^2 \approx \tilde{\sigma}_L^2$, when $a_H \gg a_L$.

In FREYA, the excitation energy ε_L is sampled from a Gaussian distribution with mean value $\underline{\varepsilon}_L$ and variance $\sigma_g^2 = \sigma_L^2$. However, because only positive values of ε_L are acceptable, the selection is iterated until $|\varepsilon_L - \underline{\varepsilon}_L| < \underline{\varepsilon}_L$. This procedure ensures that the selected value of ε_L is smaller than ε and that its mean equals $\underline{\varepsilon}_L$. But the resulting dispersion of ε_L is generally somewhat smaller than σ_L. For that reason, FREYA contains the parameter c with which one may increase the value of σ_g in order to compensate for this effect, $\sigma_g = c\,\sigma_L$. In the present study, we ignore this refinement and use $c = 1$.

APPENDIX C: BIASED TKE DISTRIBUTION

The biased distribution (38) can be written as

$$\tilde{P}(\delta\nu, \delta K) \sim e^{-\frac{1}{2}[(m_0^2 + m_\nu^2)\delta\nu^2 + 2m_{\nu K}\delta\nu\delta K + m_K^2 \delta K^2]}, \quad (C1)$$

where $m_0 \equiv 1/\sigma_0$. The corresponding biased distribution of δK is obtained by integrating over $\delta\nu$ which can easily be done

after completing the square in the exponent,

$$\left(m_0^2 + m_\nu^2\right)\delta\nu^2 + 2m_{\nu K}\delta\nu\,\delta K + m_K^2\delta K^2$$

$$= \left(m_0^2 + m_\nu^2\right)\left(\delta\nu + \frac{m_{\nu K}\delta K}{m_0^2 + m_\nu^2}\right)^2 - \left(\frac{m_{\nu K}^2}{m_0^2 + m_\nu^2} - m_K^2\right)\delta K^2. \tag{C2}$$

The integral over $\delta\nu$ can then be carried out, leaving $\tilde{P}(\delta K) \sim \exp(-\delta K^2/2\tilde{\sigma}_K^2)$ with the biased variance being given as stated in Eq. (39),

$$\tilde{\sigma}_K^2 = \left(m_K^2 - \frac{m_{\nu K}^2}{m_0^2 + m_\nu^2}\right)^{-1} = \sigma_K^2 - \frac{\sigma_{\nu K}^2}{\sigma_\nu^2 + \sigma_0^2}, \tag{C3}$$

where we have used $m_\nu^2 = \sigma_K^2/D$, $m_{\nu K} = -\sigma_{\nu K}/D$, and $\sigma_K^2 = \sigma_\nu^2/D$, with $D = |\sigma| = \sigma_\nu^2\sigma_K^2 - \sigma_\nu^2$.

[1] P. Talou *et al.*, Eur. Phys. J. A **54**, 9 (2018).
[2] FREYA: J. M. Verbeke, J. Randrup, and R. Vogt, Comp. Phys. Comm. **191**, 178 (2015); **222**, 263 (2018).
[3] CGMF: P. Talou, T. Kawano, and I. Stetcu, Tech. Rep. LA-CC-13-063, Los Alamos National Laboratory (2013).
[4] FIFRELIN: O. Litaize, O. Serot, and L. Berge, Eur. Phys. J. A **51**, 177 (2015).
[5] GEF: K. H. Schmidt, B. Jurado, C. Amouroux, and C. Schmitt, Nucl. Data Sheets **131**, 107 (2016).
[6] NICE: N. Kornilov, *Fission Neutrons: Experiments, Evaluation, Modeling and Open Problems* (Springer International Publishing, Cham, 2015).
[7] EVITA: B. Morillon and P. Romain (private communication, 2018).
[8] S. Okumura, T. Kawano, P. Jaffke, P. Talou, and S. Chiba, J. Nucl. Sci. Tech. **55**, 1009 (2018).
[9] P. Jaffke, Nucl. Sci. Eng. **190**, 258 (2018).
[10] J. Randrup, P. Talou, and R. Vogt, EPJ Web Conf. **146**, 04003 (2017).
[11] P. Jaffke, P. Möller, P. Talou, and A. J. Sierk, Phys. Rev. C **97**, 034608 (2018).
[12] A. C. Wahl, At. Data Nucl. Data Tables **39**, 1 (1988).
[13] C. Budtz-Jørgensen and H.-H. Knitter, Nucl. Phys. A **490**, 307 (1988).
[14] F.-J. Hambsch and S. Oberstedt, Nucl. Phys. A **617**, 347 (1997).
[15] E. M. Kozulin *et al.*, Instrum. Exp. Tech. **51**, 44 (2008).
[16] C. Romano, Y. Danon, R. Block, J. Thompson, E. Blain, and E. Bond, Phys. Rev. C **81**, 014607 (2010).
[17] Sh. Zeynalov, F.-J. Hambsch, and S. Oberstedt, J. Korean Phys. Soc. **59**, 1396 (2011).
[18] A. Göök, F.-J. Hambsch, and M. Vidali, Phys. Rev. C **90**, 064611 (2014).
[19] S. L. Whetstone, Jr., Phys. Rev. **131**, 1232 (1963).
[20] G. K. Mehta, J. Poitou, M. Ribrag, and C. Signarbieux, Phys. Rev. C **7**, 373 (1973).
[21] The web site for the National Nuclear Data Center is http://www.nndc.bnl.gov/exfor/exfor.htm.
[22] A. D. Carlson *et al.*, Nucl. Data Sheets **148**, 143 (2018).
[23] J. Randrup and R. Vogt, Phys. Rev. C **89**, 044601 (2014).
[24] D. Shengyao, X. Jincheng, L. Zuhua, L. Shaoming, and Z. Huanqiao, Chin. Phys. **4**, 649 (1984).
[25] R. L. Walsh *et al.*, Nucl. Phys. A **276**, 189 (1977).
[26] H. R. Bowman, J. C. D. Milton, S. G. Thompson, and W. J. Swiatecki, Phys. Rev. **126**, 2120 (1962); **129**, 2133 (1963).
[27] A. S. Vorobiev *et al.*, http://www-nds.iaea.org/exfor/servlet/X4sGetSubent?subID=41425004.
[28] O. Litaize and O. Serot, Phys. Rev. C **82**, 054616 (2010).
[29] P. Talou, B. Becker, T. Kawano, M. B. Chadwick, and Y. Danon, Phys. Rev. C **83**, 064612 (2011).
[30] J. Van Dyke, L. A. Bernstein, and R. Vogt, Phys. Rev. B **98**, 125133 (2018).
[31] R. Vogt and J. Randrup, Phys. Rev. C **96**, 064620 (2017).